X-ray emission from the exoplanet hosting LTT 1445 triple star system

Brown, A.; Froning, C.S.; Youngblood, A.; France, K.; Wilson, D.J.; Duvvuri, G.; ... ; Diamond-Lowe, H.

The Astronomical Journal, 164:206 (8pp), 2022 November https://doi.org/10.3847/1538-3881/ac8f25

X-Ray Emission from the Exoplanet Hosting LTT 1445 Triple Star System

Alexander Brown[1], Cynthia S. Froning[2], Allison Youngblood[3], Kevin France[4], David J. Wilson[4], Girish Duvvuri[1,4,5], Yamila Miguel[6], and Hannah Diamond-Lowe[7]
[1] Center for Astrophysics and Space Astronomy, University of Colorado, 389 UCB, Boulder, CO 80309, USA; Alexander.Brown@colorado.edu
[2] McDonald Observatory, University of Texas at Austin, Austin, TX 78712, USA
[3] Exoplanets and Stellar Astrophysics Lab, NASA Goddard Space Flight Center, Greenbelt, MD 20771, USA
[4] Laboratory for Atmospheric and Space Physics, University of Colorado, 600 UCB, Boulder, CO 80309, USA
[5] Department of Astrophysical and Planetary Sciences, University of Colorado, Boulder, CO 80309, USA
[6] Leiden Observatory, P.O. Box 9500, 2300 RA Leiden, The Netherlands
[7] National Space Institute, Technical University of Denmark, Elektrovej 328, DK-2800 Kgs. Lyngby, Denmark
Received 2022 June 9; revised 2022 August 12; accepted 2022 September 1; published 2022 October 20

Abstract

JWST will be able to observe the atmospheres of rocky planets transiting nearby M dwarfs. The M-dwarf triple star system LTT 1445, at a distance of 6.86 pc, hosts some of the nearest rocky terrestrial planets. These planets most likely orbit the M 3.5V star LTT 1445A. During a 28.6 ks Chandra ACIS-S3 observation we have: (i) spatially resolved and detected all three stars in the LTT 1445 system; (ii) measured the X-ray luminosity of the individual stars, including LTT 1445A, for the first time; (iii) studied the flux variability of the X-ray sources and found strong variability from the A and C components; and (iv) investigated how the coronal luminosities, temperatures, and volume emission measures vary at different activity levels. Combining these X-ray data with upcoming HST ultraviolet observations will allow a differential emission measure estimation of the star's extreme-ultraviolet spectrum, thereby facilitating modeling of the rocky planets' atmospheres.

Unified Astronomy Thesaurus concepts: M dwarf stars (982); Stellar X-ray flares (1637); Planet hosting stars (1242)

1. Introduction

Understanding what happens to rocky planets and their atmospheres in the habitable zones (HZs) of low-mass stars is currently one of the greatest astronomical challenges. The nearest Earth-mass planets in the habitable zone orbit M dwarfs, and these planets are prime targets for spectroscopic atmospheric characterization in the next decade (Shields et al. 2016; Shields 2019). M dwarfs are the most common type of star in the Galaxy, and $\geqslant 25$ % of them have planets orbiting in their habitable zones (Dressing & Charbonneau 2015). Theoretical work shows that planets around M dwarfs could be habitable despite their phase-locked orbits (Joshi 2003; Ribas et al. 2016), and dynamic modeling of transiting systems reveals that most systems permit stable orbits of Earth-mass planets long enough for the development of life, i.e., $\geqslant$1.7 Gyr (Jones & Sleep 2010). Ground-based surveys, such as MEarth (Nutzman & Charbonneau 2008) and the SPECULOOS project (Reich 2013), and space-based surveys like the Transiting Exoplanet Survey Satellite (TESS; Ricker et al. 2015) are finding and confirming nearby transiting planets orbiting M dwarfs whose atmospheres should be observable with JWST (Luque et al. 2019). The best host stars for JWST atmospheric characterization will be nearby, slowly-rotating, relatively inactive, mid–late M dwarfs with masses of 0.10–0.25 $M_{\odot}$ (Morley et al. 2017).

Over the past several years, the exoplanet community has recognized the importance of obtaining ultraviolet (UV) and X-ray spectroscopy and time-series monitoring of M dwarfs to provide a comprehensive picture of their energetic radiation environments. Surveys, such as Living with a Red Dwarf, MUSCLES, MegaMUSCLES, HAZMAT, and FUMES (Guinan et al. 2016; France et al. 2016; Froning et al. 2019; Wilson & The Mega-MUSCLES Collaboration 2021; Loyd et al. 2018; Pineda et al. 2021a), are working to characterize the radiation fields of M stars as a function of age, mass, and activity level. Such surveys are invaluable for understanding the impact of the star's high energy irradiance on the atmospheric escape, chemical evolution, observability, and potential habitability of exoplanet companions (Tilley et al. 2019; Louca et al. 2022). However, they have also shown significant scatter in the relationships between stellar parameters and the high energy radiation, flare rates, and spectral energy distributions (e.g., see Figure 3 of France et al. 2018). To interpret observations of the atmospheres of potentially habitable planets in these systems, the optimum strategy is direct panchromatic (X-ray/EUV/FUV/NUV/optical/IR) observations that can only be undertaken while the space-based capabilities of HST and Chandra/XMM-Newton remain available.

2. The LTT1445 Triple Star System

In 2018 TESS discovered a new exoplanet of high potential for JWST atmospheric characterization—a 2.87 $M_{\oplus}$ planet LTT 1445Ab in a 5.36 days orbit around the M dwarf, LTT 1445A (Winters et al. 2019). Subsequently, Winters et al. (2022) discovered a second 1.54 $M_{\oplus}$ exoplanet in a 3.12 day orbit and improved estimates of the physical properties for both planets. At a distance of 6.864 ± 0.001 pc (Gaia Collaboration et al. 2021), LTT 1445A is the nearest known transiting exoplanet system orbiting an M dwarf, which will substantially improve the ability of JWST to detect atmospheric features and direct thermal emission in a reasonable observing time. LTT 1445A is an approved JWST target for such an observation

(program GO#02708; PI Berta-Thompson). Thus, as noted by Winters et al. (2019), "based on the known occurrence rates of planets orbiting M dwarfs, it is unlikely that we will detect a small planet more favorable for atmospheric characterization." It is also bright enough for radial-velocity follow-up to determine planetary masses and gravities (Winters et al. 2022).

LTT 1445 is a hierarchical triple star system with LTT 1445A separated by 7″ from the tighter 36 year period visual binary BC. The astrometric orbital motions of all three stars were measured by Winters et al. (2019). LTT 1445A is an M3.5 V star with a mass of $0.257 \pm 0.014\ M_{\odot}$. The B and C components have masses of $0.215 \pm 0.014\ M_{\odot}$ and $0.161 \pm 0.014\ M_{\odot}$, which correspond to spectral types of M3.5 V and M4 V, when compared to masses and spectral types of other M-dwarf exoplanet hosts (see e.g., Pineda et al. 2021b). For comparison, Reid et al. (2004) assigned spectral types of M3, M3.5, and M4 to A, B, and C, respectively. Winters et al. (2019) estimated the bolometric luminosity of A to be $3.04 \pm 0.12 \times 10^{31}$ erg s^{-1} . Scaling from the K magnitudes of the three stars ($K = 6.50$, 6.81, 7.33 for A, B, and C, respectively), the bolometric luminosities of the B and C components are 2.28 and 1.41×10^{31} erg s^{-1}. These values are entirely consistent with published values for M dwarfs with similar masses (Pineda et al. 2021b).

The mass and radius measurements of LTT 1445Ab ($2.87 \pm 0.26\ M_{\oplus}$; $1.305 \pm 0.066\ R_{\oplus}$) and LTT 1455Ac ($1.54 \pm 0.20\ M_{\oplus}$; $1.147 \pm 0.055\ R_{\oplus}$) indicate that both are likely to be terrestrial with Earth-like compositions (Winters et al. 2022). These planets lie interior to the habitable zone around the star with the cooler LTT 1445Ab having an equilibrium temperature of 424 ± 21 K, which is intermediate to other rocky planets such as GJ1132b and TRAPPIST1-b. Although the known LTT 1445A planets are likely not habitable, they remain excellent targets for detailed atmospheric studies with JWST; plus, given the frequency of multiple small planets around M dwarfs, later TESS or ground-based radial-velocity observations may reveal other planets in HZ orbits. To properly interpret these and other studies of LTT 1445Ab and Ac, the high energy X-ray/UV context that governs exoplanet atmospheric properties must be established.

The LTT 1445 triple system was detected as a reasonably bright ROSAT PSPC source at a count rate of 0.25 cts s^{-1} (Boller et al. 2016), but it was unclear how the X-ray signal is distributed between the three stars. Ground-based spectra (Winters et al. 2019) indicate that Balmer Hα emission is detected from the BC binary, suggesting that at least one of these stars is magnetically active. Hα from the A component is in absorption, suggesting that this star is less likely to be the dominant X-ray emitter.

3. Chandra Observations

The LTT 1445 system was observed by the Chandra X-ray Observatory on 2021 June 5 using the ACIS-S3 back-illuminated detector in $\frac{1}{4}$subarray mode and VFAINT telemetry mode (ObsID 23377; PI Brown). The observation started at 01:41:32 UT and lasted 28.59 ks. The spatial resolution of ACIS is just under 1″ (nominally 0.″84 at 50% of the PSF peak but the CCD pixel size is only 0.″49) and is sufficient to resolve LTT 1445A from BC. The photon-counting capability of ACIS allows study of coronal flaring during the observation and thus provides additional information on the high energy and overall SED variability for the stars.

4. Data Analysis

The ACIS-S data were analyzed using standard CIAO (Fruscione et al. 2006) techniques on the standard pipeline-processed data set obtained from the mission archive. CIAO version 4.13 was used. Analysis was performed on data filtered to contain only events in the energy range 0.3–10 keV. Events above 10 keV are unlikely to be of stellar origin and are usually due to high energy particles. ACIS now has minimal sensitivity below 0.7 keV due to contaminant buildup on the optical blocking filters.[8] Energy filtering further reduced the already low detector background signal. Source events were extracted using circular regions: for LTT 1445A and the combined BC source a standard 2.″5 radius was used. For exploring the individual contributions of the B and C components smaller 1.″0 and 0.″75 radii circles were used.

4.1. Source Detection and Identification

Three X-ray sources are present in the ACIS image—one well separated source at the position of LTT 1445A and a barely resolved pair of sources coincident with LTT 1445BC (see Figure 1). The northwest source within the BC pair is by far the strongest X-ray emitter within the system. LTT 1445A at a distance of 7″ was easily separated from BC. However, it was surprising that the LTT 1445BC binary was spatially resolved by ACIS, because the preliminary astrometric orbit estimated for the BC binary by Winters et al. (2019) implied that the two stars should have been far too close to be resolved in 2021 June. This discrepancy means that it is not possible from the Chandra data alone to associate the X-ray sources to the individual B and C components. The CIAO program *wavedetect* was unable to separate the BC X-ray source but instead identified a single highly elliptical source encompassing both stars. The wavedetect centroid position for LTT 1445A agreed well with the proper-motion-corrected GAIA EDR-3 position (Gaia Collaboration et al. 2016, 2021) with the offset between the two positions being only 0.″8.

Fortunately, LTT 1445 was observed by the HST WFC3/UVIS instrument on 2021 September 26 and 29 using the F814W filter (program 16503; PI Winters; Obsids iejra2*, iejr03*). The passband of the F814W filter extends from 7000 Å to 9600 Å. These trailed images clearly show that the three LTT 1445 components lie along the SE-NW orbit in the order A-B-C, with A being the optically brightest and C the faintest. Even though the stellar images are trailed, rather than point-like, it is still possible to estimate the separations well enough to remove any ambiguities in the X-ray data. Thus, LTT 1445C is the brightest X-ray source in the system with ∼1200 counts recorded from the full 28.6 ks observation, while the B source has ∼250 counts and the A source is the weakest with ∼225 counts. In the X-ray image the A and C sources are separated by 8.″2, the A and B sources by 7.″0, and the B and C sources by 1.″25—these values are all in agreement with the optical imaging almost 4 months later. This location of C so far northwest of B is well beyond the maximum extent of the Winters et al. (2019) orbit, which has a maximum separation of 0.″6 in this direction. Additional optical data will undoubtedly resolve this discrepancy but any physical properties of this binary published in the 2019 paper should be treated with

[8] See http:/cxc/harvard.edu/proposer/POG/html/chap6.html.

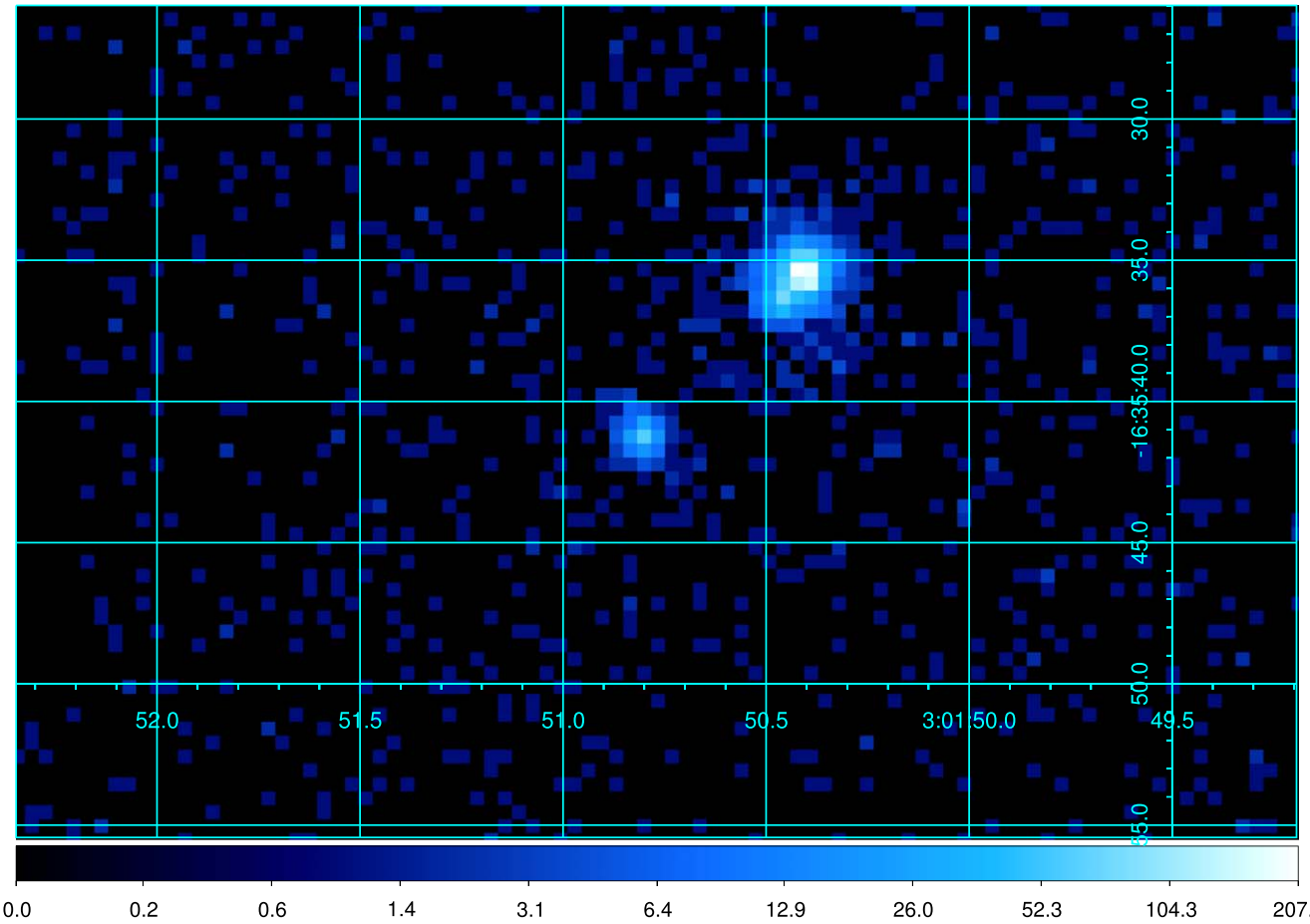

Figure 1. The reconstructed Chandra ACIS-S3 image of LTT 1445. North is up and east to the left. The coordinate grid spacing is 5″ in decl. and 0.5 s of time in R.A. The color wedge illustrates the integrated number of counts per 0.″5 pixel. LTT 1445A is the fainter source at the center of the image with the brighter resolved BC binary to the NW.

caution. However, none of the most critical stellar parameters in Winters et al. (2019) rely on the BC orbit.

4.2. X-Ray Variability

After applying a barycentric correction to the ACIS data, X-ray light curves were constructed using the CIAO command dmextract using a variety of binning timescales and extraction region sizes. The light curve for LTT 1445A is shown in the upper panel of Figure 2 and shows that the X-ray emission from A is highly variable with a large flare present. The combined BC light curve and the scaled light curve from the PSF core of LTT 1445B are shown in the lower panel. The BC light curve shows significant variability throughout with the flaring originating from LTT 1445C. Even though LTT 1445B lies on the PSF wings of the variable C source, the signal measured from the PSF core of B does not show significant variability aligned with major changes in the combined BC signal.

The LTT 1445A light curve has three distinct time intervals: an initial 12 ks "Quiescent" segment with a very low count rate, then a 7 ks long "Flare" outburst with multiple impulsive events, followed by just under 12 ks with an "Elevated" count rate at ∼10 times the quiescent level. At the end of the flare the count rate falls to the quiescent level before rising again. The reality of this variability is secure because the overall signal allows the LTT 1445A source region to be accurately positioned and the simultaneously recorded signal from the BC binary shows that ACIS was operating correctly. Data were extracted for the different time intervals and analyzed individually. Similarly, the largest flare from the BC source was also separated from the rest of those data.

4.3. Spectral Analysis

Spectral fitting was performed using XSPEC V12.12 (Arnaud 1996; Dorman et al. 2003) to derive X-ray luminosities for all three sources and to estimate the coronal characteristic temperature and volume emission measure. The data for the A and BC components was split into different time intervals and the time variable plasma properties investigated. In most cases a single temperature (1-T) VAPEC model (Smith et al. 2001) was sufficient to model the binned spectrum. However, for the "Flare" interval of the BC source a two-temperature model was heavily favored with a reduced χ^2 of 1.26, compared to 2.2 for a 1-T fit. For all fits, the interstellar hydrogen column density was fixed at 1×10^{19} cm^{-2}; this value consistently provided better χ^2 values than lower interstellar columns. Generally, ACIS spectra cannot constrain low column densities well. Initial subsolar abundances were assumed as starting values based on results from M dwarf X-ray grating spectra analyses including Raassen et al. (2003), van den Besselaar et al. (2003), Güdel et al. (2004), and Wargelin et al. (2008). Most importantly, the Fe abundance

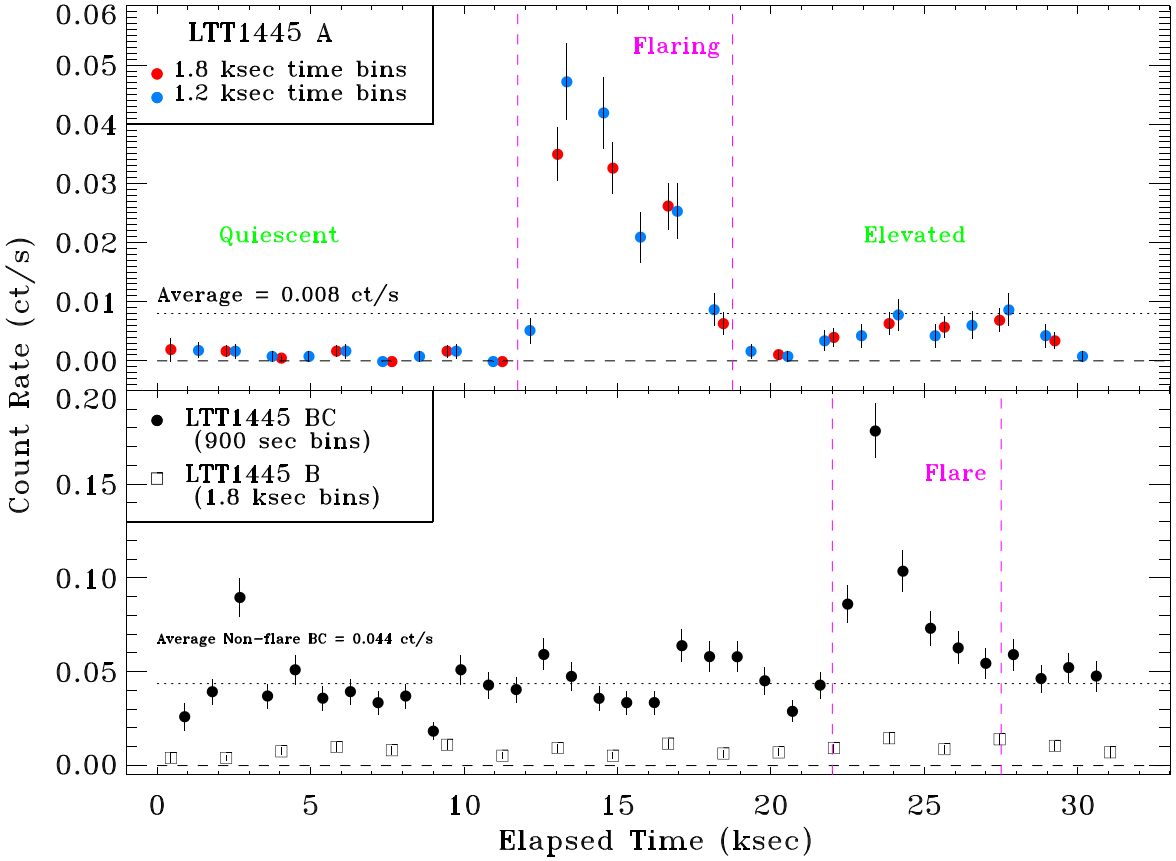

Figure 2. The Chandra ACIS-S3 light curves for the LTT 14445 X-ray sources. Upper panel: the light curve for LTT 1445A with different activity level segments separated by vertical dashed lines. Two different binning intervals (1.2 ks (20 minutes) and 1.8 ks (30 minutes) are plotted to better track the variability during the flare outburst. Lower panel: the combined signal from the BC binary with 900 sec binning (filled dots), and the signal from the B component alone extracted using a small 1.″0 radius circular region and then scaled to recover the likely full PSF signal (open squares). For the BC source the largest flare was also measured separately.

Table 1
Coronal X-Ray Properties for LTT 1445A

	A—Full Data Set	A—Flare	A—Elevated	A—Quiescent
Exposure (ks)	28.6	6.66	11.6	12.2
Source Counts (ct)	228	177	46	4.9
Count Rate (ct ks^{-1})	8.0 ± 0.5	26.6 ± 2.0	4.0 ± 0.6	0.4 ± 0.2
f_X (10^{-13} erg cm^{-2} s^{-1})	1.52 ± 0.10	3.61 ± 0.27	0.66 ± 0.10	0.066 ± 0.033
log L_X	26.93 ± 0.03	27.31 ± 0.03	26.57 ± 0.07	$25.57^{+0.18}_{-0.30}$
log L_X/L_{bol}	-4.55 ± 0.04	-4.17 ± 0.04	-4.91 ± 0.07	$-5.90^{+0.2}_{-0.3}$
kT_1 (keV)	0.63 ± 0.08	1.02 ± 0.10	0.59 ± 0.29	⋯
norm1 (10^{-4})	1.16 ± 0.36	2.24 ± 0.80	0.38 ± 0.34	⋯
VEM_1 (10^{49} cm^3)	0.52 ± 0.16	1.00 ± 0.36	0.17 ± 0.15	⋯
Fe Abundance	0.20 ± 0.07	0.42 ± 0.14	Fixed 0.4 solar	⋯
Red. χ^2	0.87	0.88	1.7	⋯

was set to 0.4 relative to the XSPEC Anders & Grevesse (1989) solar abundances. The Ca and Ni abundances were tied to that of Fe. For C, N, O, Ne, Mg, Al, Si , S, and Ar relative abundances of 1.0, 0.75, 0.3, 0.8, 0.5, 0.5, 0.65, 0.4, and 0.55 were adopted. Most of these abundances have little influence in the fitting of ACIS CCD spectra in XSPEC. After model fitting with fixed abundances, the Fe abundance was allowed to vary to see if this provided a smaller reduced χ^2 value.

The X-ray properties for LTT 1445A are listed in Table 1. The X-ray fluxes and luminosities listed are for the 0.3-10.0 keV energy range. XSPEC fits were performed for the full data set and the "Flare" and "Elevated" portions of the light curve. The initial "Quiescent" interval contains too few counts for spectral fitting but the X-ray flux and luminosity were estimated assuming that the coronal temperature was similar to that during the "Elevated" time interval. The range in the X-ray emission from LTT 1445A is large with the count rate going from 0.4 counts ks^{-1} in quiescence to 47.2 counts ks^{-1} at the flare peak—thus, varying by a factor of ∼100. However, the quiescent X-ray luminosity is at a low level of 3.7×10^{25} erg s^{-1} .

The X-ray properties for LTT 1445BC are listed in Table 2. XSPEC fits were performed for the full data set and both "Flare" and "Nonflare" portions of the light curve. However, given the continuous variability of the BC source, both these segments almost certainly contain numerous flares. For the

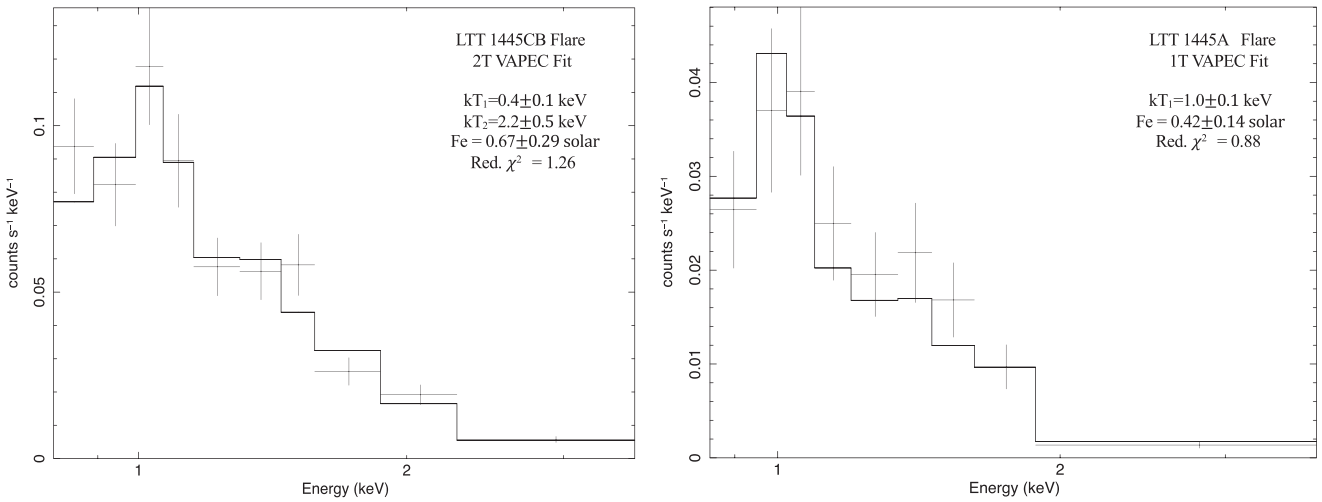

Figure 3. Examples of XSPEC spectral fitting to Chandra CCD-resolution spectra. These figures demonstrate the fitting framework within XSPEC. The spectral data with associated error bars are overlaid on the final model shown as a histogram. Right panel: a one-temperature (1-T) fit to the flare spectrum of LTT 1445A grouped with 17 events per channel. Left panel: a two-temperature (2-T) fit to the flare spectrum of LTT 1445 CB grouped with 40 events per channel.

Table 2
Coronal X-Ray Properties for LTT 1445BC

	CB—Full Data Set	CB—Flare	CB—Nonflare	C	B
Exposure (ks)	28.6	5.2	23.4	28.6	28.6
Source Counts (ct)	1,468	470	997	1218	250
Count Rate (ct ks^{-1})	51.3 ± 1.3	89.9 ± 4.2	42.7 ± 1.4	42.5 ± 1.2	8.7 ± 0.6
f_X (10^{-13} erg cm^{-2} s^{-1})	9.4 ± 0.2	20.2 ± 0.9	7.3 ± 0.2	7.3 ± 0.2	1.7 ± 0.1
log L_X	27.72 ± 0.02	28.06 ± 0.02	27.61 ± 0.01	27.62 ± 0.01	26.97 ± 0.03
log L_X/L_{bol}	-3.84 ± 0.062	-3.51 ± 0.02	-3.95 ± 0.01	-3.53 ± 0.01	-4.39 ± 0.03
kT_1 (keV)	0.77 ± 0.03	0.38 ± 0.10	0.76 ± 0.03		
norm1 (10^{-4})	4.1 ± 1.7	7.3 ± 4.5	4.1 ± 0.3		
VEM_1 (10^{49} cm^3)	1.86 ± 0.71	3.27 ± 2.02	1.84 ± 0.13		
kT_2 (keV)	⋯	2.2 ± 0.5	⋯		
norm2 (10^{-4})	⋯	5.0 ± 1.5	⋯		
VEM_2 (10^{49} cm^3)	⋯	2.23 ± 0.66	⋯		
Red. χ^2	1.23[a]	1.26[b]	1.16[c]		

Notes.
[a] Fitted abundances: Fe: 0.38 ± 0.08, Si: 0.50 ± 0.16, Ne: 1.26 ± 0.56.
[b] Fitted abundances: Fe: 0.67 ± 0.29.
[c] Fe abundance fixed to 0.4 solar.

combined CB measurements, the summed bolometric luminosities are used to estimate log L_X/L_{bol}. The properties of the individual C and B sources are also estimated, based on the count levels at the peak of the PSFs.

Examples of the spectral fitting within XSPEC are shown in Figure 3. The binning of the spectra is a delicate balance between maintaining sufficient events in each spectral channel while providing enough valid channels to solve for the number of fit parameters. The presence of flaring plasma, clearly seen in the light curves, is confirmed by the coronal characteristic temperatures measured by the 1-T fits, which are in the range 0.6–0.8 keV (7–9 MK). Temperatures at this level are hotter than typical quiescent coronal temperatures of low activity M dwarfs (0.3–0.4 keV; 3.5–5 MK; A. Brown et al. 2022, in preparation) and indicate a significant presence of flaring and cooling post-flare plasma in the coronae of LTT 1445 A and C. This is emphasized by the 2-T fit to the LTT 1445CB "Flare," where comparable amounts of cool 0.38 keV (4.5 MK) and very hot 2.2 keV (25 MK) plasma are present. The corresponding 1-T coronal temperature was 1.05 ± 0.07 keV. Using a 1-T model can often result in a parameterization favoring intermediate values when a wide range of plasma conditions are present.

5. Discussion

5.1. X-Ray Activity Levels

The measured X-ray luminosities for the three stars in the LTT 1445 system can be compared to the behavior of the wider solar neighborhood M dwarf population. Stellar rotation is the dominant factor controlling magnetic activity on M dwarfs (Noyes et al. 1984; Pizzolato et al. 2003; West et al. 2015; Magaudda et al. 2020). Initially, young rapidly rotating M dwarfs show saturated coronal emission with log $L_X/L_{bol} \simeq$-3 . Then, as rotation slows, the X-ray luminosity decreases. Wright et al. (2018, 2011) provide a detailed study of the relationship between X-ray luminosity in the ROSAT 0.1–2.4 keV energy range and stellar rotation for a wide range of dwarf stars with F-G-K-M spectral types. They showed that the tightest correlations involved the Rossby number ($R_0 = P_{rot}/\tau$, where

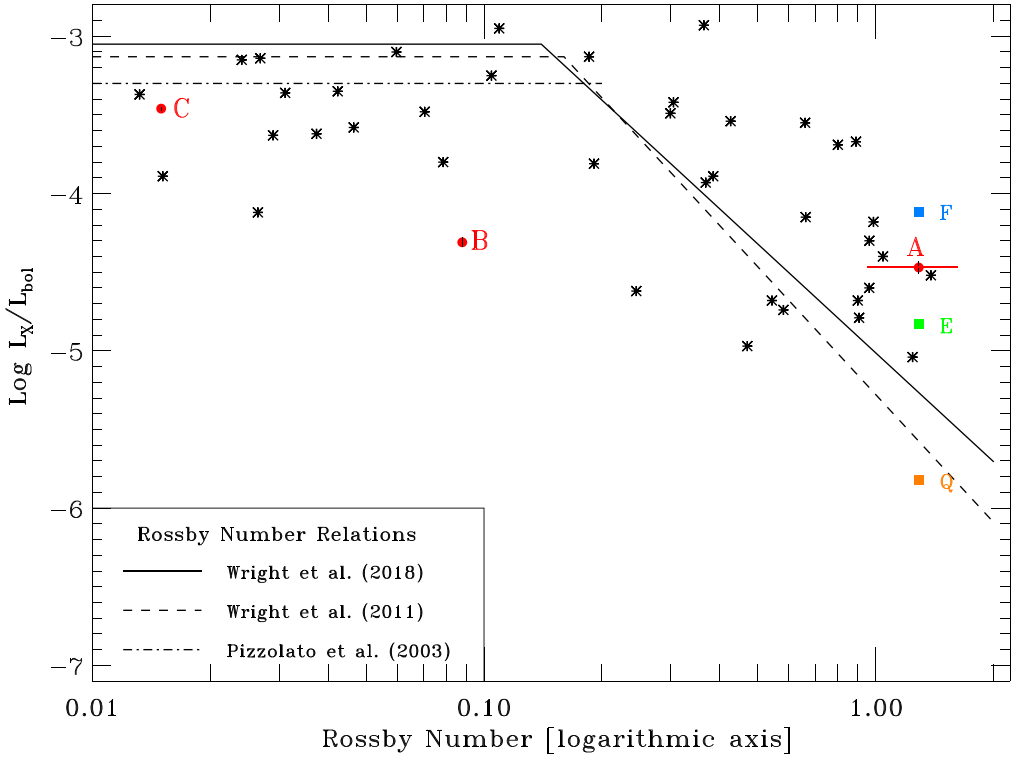

Figure 4. X-ray to bolometric luminosity ratios for the LTT 1445 X-ray sources as a function of Rossby number. Mean X-ray emission for each star is shown as red circles. The different activity levels of LTT 1445A are shown as filled squares: quiescent (Q—orange), elevated (E—green), and flare (F—blue). The nearby M-dwarf sample included in Wright et al. (2018) and Wright et al. (2011) are shown as black asterisks. The empirical relationships between the X-ray to bolometric luminosity ratio and Rossby number (rotation period/convective turnover timescale) derived by Wright et al. (2018, 2011) from larger samples of F-M type dwarfs are plotted as solid and dashed lines, respectively. The M-dwarf saturated activity level of Pizzolato et al. (2003) is shown as a dotted–dashed line.

τ is the convective turnover time), rather than the rotation period (P_{rot}) alone. The relationships discussed by Wright et al. (2018) and Wright et al. (2011) are shown in Figure 4. The declines from saturated emission start at $R_0 = 0.14$ and 0.16. As a guide to the range of coronal activity detected, the sample of nearby M dwarfs included in these papers are plotted on Figure 4. The Rossby numbers for all these stars were recalculated using Equation (5) of Wright et al. (2018).

Winters et al. (2022) estimated the rotation periods of the A, B, and C components to be 85 ± 22, 6.7 and 1.4 days, respectively, which correspond to Rossby numbers of 1.287 ± 0.333, 0.088, and 0.015. Therefore, LTT 1445 B and C should be fast rotators and show saturated activity. The observed X-ray to bolometric luminosity ratios for the three LTT 1445 stars are plotted in Figure 4, as well as those for different activity levels shown by LTT 1445 A. These X-ray luminosities were converted from the Chandra 0.3–10.0 keV energy range to the ROSAT band using PIMMS[9] and the spectral properties listed in Tables 1 and 2. Converting from the Chandra to ROSAT energy band increases the X-ray luminosity by a factor that is temperature dependent (29.7% increase at 0.4 keV, 20.6% increase at 0.6 keV, 17.9% increase at 0.8 keV, and 11.7% at 1.1 keV). Interestingly, the large observed range in the X-ray emission from LTT 1445A covers the wide spread in log L_X/L_{bol} seen for other M dwarfs, which provides further support to the suggestion that much of that spread is due to flaring variability. While the L_X/L_{bol} for LTT 1445C lies 0.5 dex below the saturation limit of Wright et al. (2018), it is less than 0.2 dex below that of Pizzolato et al. (2003).

While the A and C components have X-ray emission in agreement with the activity-R_0 relationships, the X-ray emission from the B component is a factor of ∼20 below the Wright et al. (2018) saturated level for a star with a 6.7 day rotational period. The observed L_X/L_{bol} for LTT 1445B corresponds to a rotation period of ∼45 days on the relationship of Wright et al. (2018). However, many other M dwarfs with similar Rossby numbers also lie significantly below the nominal saturated level and it is unclear whether LTT 1445B was observed during quiescence and future observations will show brighter coronal emission or if it is indeed a more slowly rotating star.

5.2. Flares and Coronal Variability

An important factor influencing the atmospheric stability and photochemistry of extrasolar planets is temporal variability of the energetic incident radiation. Impulsive magnetic flares can be related to energetic particle ejections. Segura et al. (2010) showed that energetic particle deposition into the atmosphere of an Earth-like planet during large M-dwarf flares can lead to significant atmospheric ozone depletion (⩾90% for extreme flares). This alters the atmospheric chemistry and increases the penetration depth of UV photons that are damaging to surface life (Tilley et al. 2019). Most M stars exhibit significant X-ray/UV variability, even for older systems (see e.g France et al. 2020), as evidenced by the many flares seen in MUSCLES observations (Loyd et al. 2018). These flares can be comparable to or exceed the quiescent flux

[9] The Portable Interactive Multi-Mission Simulator, http:/cxc/harvard.edu/toolkit/pimms/jsp.

of the star (Loyd et al. 2018; Froning et al. 2019). On the other hand, the intense flare flux may be needed to spur the formation of life, as the low quiescent NUV flux from M stars may be insufficient to drive UV-sensitive prebiotic nucleotide synthesis (Ranjan et al. 2017; Rimmer et al. 2018).

Even though the X-ray luminosity of LTT 1445A is weak, the range of variability is very large. This implies that the high energy irradiance on its planets will be highly variable and lead to stochastic atmospheric changes. Our 28.6 ks view of the X-ray emission from LTT 1445A provides only a limited window into the flaring duty cycle. Fortunately, a longer 50 ks ACIS-S observation is scheduled in the second half of 2022 (PI: Predehl; ObsID: 25993), which should provide improved insights into the temporal variability of X-ray emission from this star.

5.3. Stellar Spectral Energy Distribution

Knowledge of the complete stellar SED is vital when modeling the surface and atmospheric conditions of any exoplanet and X-ray observations alone cannot provide a complete description of the SED. Optical/IR photons are the dominant overall heating source that determines the location of the habitable zone around the star. Ultraviolet stellar radiation drives atmospheric heating and chemistry on Earth-like planets, while EUV/X-ray radiation forces thermospheric heating and atmospheric escape and erosion. Most of the stellar SED can be observed directly except for the extreme ultraviolet (EUV; $100 \leqslant \lambda \leqslant 911$ Å), which must be modeled. EUV photons from the central star are an important source of atmospheric heating and ionization on all types of extrasolar planets. For terrestrial atmospheres, increasing the EUV flux to levels estimated for the young Sun (~1 Gyr; Ayres 1997) can increase the temperature of the thermosphere by a factor of $\geqslant 10$ (Tian et al. 2008), potentially causing significant and rapid atmospheric mass loss. Estimates of the incident EUV flux are therefore important to the long-term stability of an exoplanetary atmosphere; however, direct measurement of the complete EUV irradiance spectrum is extremely difficult because of a lack of EUV space observatories and because attenuation by interstellar hydrogen prevents detailed characterization for most stars except the Sun. Stellar EUV emission is a combination of emission from both transition region ($\sim 10^5$ K) plasma and coronal ($\geqslant 10^6$ K) plasma. Other emission lines from these two thermal regions can be observed directly in the FUV and X-ray spectral regions. Therefore, the most accurate and reliable method to calculate the EUV radiation field is via the combined differential emission measure (DEM) analysis of FUV and X-ray spectra (Louden et al. 2017).

We intend to model the CCD-resolution spectra measured by Chandra in combination with planned future HST FUV/NUV spectra (Program 16701, PI Youngblood; Program 16722, PI Diamond-Lowe) using the MCMC DEM modeling technique (Duvvuri et al. 2021), which is currently being used to analyze the SEDs of other M-dwarf exoplanet host stars. This should provide full irradiance spectra that can be used in atmospheric modeling of the exoplanets orbiting LTT 1445A.

6. Conclusions

Chandra ACIS-S observations have detected and resolved the coronal X-ray emission from all three stars in the LTT 1445 system, including from the exoplanet host star LTT 1445A. The dominant X-ray emitter in the system is the lowest mass star LTT 1445C, which is the most likely source of 1.4 day period optical variability seen in TESS light curves. The Chandra observations of LTT 1445A provide further evidence that the coronal emission of older, slowly-rotating M dwarfs can be highly variable and the coronal emission already seen from LTT 1445A suggests that this star may have interesting influences on the atmospheres of its exoplanets. During the observed flare the X-ray luminosity is only a factor of 10 below the saturated activity level expected from young, very active stars, even though LTT 1445A is thought to be slowly rotating. More extensive studies of its X-ray activity should provide a clearer picture of the range of coronal emission from all three mid-M dwarfs in the LTT 1445 system.

We thank the referee for useful comments and suggested additions to this paper. This research has used data obtained by the Chandra X-ray Observatory and software provided by the Chandra X-ray Center (CXC) in the CIAO application package. This work was supported by Chandra grant GO1-22005X to the University of Colorado. An HST/WFC3 optical image of the LTT 1445 system was obtained from the Mikulski Archive for Space Telescopes (MAST) at the Space Telescope Science Institute, which is operated by the Association of Universities for Research in Astronomy Inc., under NASA contract NAS5-26555.

We acknowledge the invaluable resources of NASA's Astrophysics Data System and the SIMBAD/VIZIER databases operated by CDS, Strasbourg, France (Wenger et al. 2000).

Facilities: CXO (ACIS), HST (WFC3).

Software: CIAO (Fruscione et al. 2006), XSPEC (Arnaud 1996), IDL (Ver. 8.8; Excelis Visual Information Solutions, Boulder, CO).

ORCID iDs

Alexander Brown https://orcid.org/0000-0003-2631-3905
Cynthia S. Froning https://orcid.org/0000-0001-8499-2892
Allison Youngblood https://orcid.org/0000-0002-1176-3391
Kevin France https://orcid.org/0000-0002-1002-3674
David J. Wilson https://orcid.org/0000-0001-9667-9449
Girish Duvvuri https://orcid.org/0000-0002-7119-2543
Hannah Diamond-Lowe https://orcid.org/0000-0001-8274-6639

References

Anders, E., & Grevesse, N. 1989, Geochim. Cosmochim. Acta, 53, 197
Arnaud, K. A. 1996, in ASP Conf. Series., 101 Astronomical Data Analysis Software and Systems V, ed. G. Jacoby & L. Barnes (San Francisco, CA: ASP), 17
Ayres, T. R. 1997, ApJ, 491, 876
Boller, T., Freyberg, M. J., Truemper, J., et al. 2016, A&A, 588, A103
Dorman, B., Arnaud, K. A., & Gordon, C. A. 2003, BAAS, 35, 641
Dressing, C. D., & Charbonneau, D. 2015, ApJ, 807, 45
Duvvuri, G. M., Pineda, J. S., Berta-Thompson, Z. K., et al. 2021, ApJ, 913, 40
France, K., Arulanantham, N., Fossati, L., et al. 2018, ApJS, 239, 16
France, K., Duvvuri, G., Egan, H., et al. 2020, AJ, 160, 237
France, K., Loyd, R. O. P., Youngblood, A., et al. 2016, ApJ, 820, 89
Froning, C. S., Kowalski, A., France, K., et al. 2019, ApJL, 871, L26
Fruscione, A., McDowell, J. C., Allen, G. E., et al. 2006, SPIE, 6270, 62701V
Gaia Collaboration, Brown, A. G. A., Vallenari, A., et al. 2021, A&A, 649, A1
Gaia Collaboration, Prusti, T., de Bruijne, J. H. J., et al. 2016, A&A, 595, A1
Güdel, M., Audard, M., Reale, F., Skinner, S. L., & Linsky, J. L. 2004, A&A, 416, 713
Guinan, E. F., Engle, S. G., & Durbin, A. 2016, ApJ, 821, 81

Jones, B. W., & Sleep, P. N. 2010, MNRAS, 407, 1259
Joshi, M. 2003, AsBio, 3, 415
Louca, A. J., Miguel, Y., Tsai, S.-M., et al. 2022, arXiv:2204.10835
Louden, T., Wheatley, P. J., & Briggs, K. 2017, MNRAS, 464, 2396
Loyd, R. O. P., France, K., Youngblood, A., et al. 2018, ApJ, 867, 71
Luque, R., Pallé, E., Kossakowski, D., et al. 2019, A&A, 628, A39
Magaudda, E., Stelzer, B., Covey, K. R., et al. 2020, A&A, 638, A20
Morley, C. V., Kreidberg, L., Rustamkulov, Z., Robinson, T., & Fortney, J. J. 2017, ApJ, 850, 121
Noyes, R. W., Hartmann, L. W., Baliunas, S. L., Duncan, D. K., & Vaughan, A. H. 1984, ApJ, 279, 763
Nutzman, P., & Charbonneau, D. 2008, PASP, 120, 317
Pineda, J. S., Youngblood, A., & France, K. 2021a, ApJ, 911, 111
Pineda, J. S., Youngblood, A., & France, K. 2021b, ApJ, 918, 40
Pizzolato, N., Maggio, A., Micela, G., Sciortino, S., & Ventura, P. 2003, A&A, 397, 147
Raassen, A. J. J., Mewe, R., Audard, M., & Güdel, M. 2003, A&A, 411, 509
Ranjan, S., Wordsworth, R. D., & Sasselov, D. D. 2017, ApJ, 843, 110
Reich, E. S. 2013, Natur, 502, 606
Reid, I. N., Cruz, K. L., Allen, P., et al. 2004, AJ, 128, 463
Ribas, I., Bolmont, E., Selsis, F., et al. 2016, A&A, 596, 111
Ricker, G. R., Winn, J. N., Vanderspeck, R., et al. 2015, JATIS, 1, 014003
Rimmer, P. B., Xu, J., Thompson, S. J., et al. 2018, SciA, 4, 3302
Segura, A., Walkowicz, L. M., Meadows, V., Kasting, J., & Hawley, S. 2010, AsBio, 10, 751
Shields, A. L. 2019, ApJS, 243, 30
Shields, A. L., Ballard, S., & Johnson, J. A. 2016, PhR, 663, 1
Smith, R. K., Brickhouse, N. S., Liedahl, D. A., & Raymond, J. C. 2001, ApJL, 556, L91
Tian, F., Kasting, J. F., Liu, H.-L., & Roble, R. G. 2008, JGR, 113, E5
Tilley, M. A., Segura, A., Meadows, V., Hawley, S., & Davenport, J. 2019, AsBio, 19, 64
van den Besselaar, E. J. M., Raassen, A. J. J., Mewe, R., et al. 2003, A&A, 411, 587
Wargelin, B. J., Kashyap, V. L., Drake, J. J., Garcia-Alvarez, D., & Ratzlaff, P. W. 2008, ApJ, 676, 610
Wenger, M., Ochsenbein, F., Egret, D., et al. 2000, A&AS, 143, 9
West, A. A., Weisenburger, k. L., Irwin, J., et al. 2015, ApJ, 812, 3
Wilson, D. & The Mega-MUSCLES Collaboration 2021, in The 20.5th Cambridge Workshop on Cool Stars, Stellar Systems, and the Sun (CS20.5) (Cambridge, MA: Harvard), 253
Winters, J. G., Cloutier, R., Medina, A. A., et al. 2022, AJ, 163, 168
Winters, J. G., Medina, A. A., Irwin, J. M., et al. 2019, AJ, 158, 152
Wright, N. J., Drake, J. J., Mamajek, E. E., & Henry, G. W. 2011, ApJ, 743, 48
Wright, N. J., Newton, E. R., Williams, P. K. G., Drake, J. J., & Yadav, R. K. 2018, MNRAS, 479, 2351